Additive Manufacturing Letters 7 (2023) 100176

Contents lists available at ScienceDirect

Additive Manufacturing Letters

journal homepage: www.elsevier.com/locate/addlet

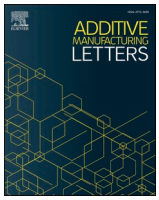

Short Communication

On the development of twinning-induced plasticity in additively manufactured 316L stainless steel

D. Della Crociata, I. Maskery *, R. Hague, M. Simonelli

Centre for Additive Manufacturing, University of Nottingham, Nottingham NG8 1BB, UK

ARTICLE INFO

Keywords:
Powder bed fusion
Twinning-induced plasticity
Stainless steel
Phase transformation

ABSTRACT

A report on twinning-induced plasticity in 316L stainless steel manufactured by metal additive manufacturing (AM) is presented. A tapered tensile test geometry was used which enabled the investigation of twin formation over a range of strain levels in a single specimen. Hardness and twinning concentration were observed to increase with strain up to peak values of 380 ± 10 HV and 28 ± 4%, respectively. Furthermore, twin formation was found to be regulated by grain size and crystal texture. This methodology can be applied to new AM materials development and will inform the design of energy-absorbing structures that maximise the benefits of AM design and strain-hardenable materials.

Introduction

Additive manufacturing (AM) enables the production of complex and customised products, and has become a key technology in the automotive, aerospace and medical sectors. Over the last decade, AM research focus has shifted from fundamental problems such as ensuring geometrical accuracy and eliminating defects (the main one being porosity), to more practical issues, such as creating products with highly desirable mechanical properties. For metallic alloys, the most widely used AM production route is powder bed fusion-laser beam (PBF-LB) [1].

PBF-LB gives rise to non-equilibrium microstructures distinct from those formed by traditional processes such as forging and rolling. This is due to the fast solidification rates and repeated heating-cooling cycles inherent to the manufacturing process [2,3]. A major challenge facing PBF-LB is that, while laser processing parameters are known to affect the microstructure, the phenomena are not sufficiently understood to allow complete microstructural control during manufacture [4].

This study focusses on 316L stainless steel, which has widespread commercial use, is known to have PBF-LB manufacturability, and has desirable characteristics including high strength, ductility and strain-hardening behaviour thanks to twinning induced plasticity (TWIP) [5,6]. PBF-LB 316L has attracted interest for use in crash protection applications [7–9], where the TWIP extends the plastic deformation and therefore increases energy absorption before failure.

While the high strength of PBF-LB 316L is attributed to the high dislocation density and fine grain size via the Hall-Petch effect [5,10], its high ductility is linked to a strain-hardening mechanism. The phenomenon is regulated by the hierarchical microstructure of PBF-LB 316L that spans nearly six orders of magnitude [11]. Solute segregation along cellular walls (mainly Cr and Mo, but also Si, O and Mn [12]) and low-angle grain boundaries increase dislocation pinning and promote twinning [11]. Twins oppose dislocation movement, providing an additional strength increase [13,14].

Although the mechanisms of strain-hardening in PBF-LB 316L are mostly understood, the development of the microstructure under strain has not been given much attention. To address this, our methodology utilises a tapered tensile specimen geometry with varying cross-section in the gauge section. The tapered geometry was prepared so that a single test would generate all the necessary information on twinning, since the local stress and strain vary along the length of the specimen. The angle of taper was kept small to keep the stress system as simple and as near to a conventional tensile test as possible [15]. Comparison with numerical predictions of the local strain made by finite element (FE) modelling then provides a complete picture of strain-induced microstructural transformation. This study enables future work to focus on the link between PBF-LB process parameters, microstructure and the resulting strain-hardening behaviour.

Material and methods

Test specimens of 316L stainless steel were fabricated using a

* Corresponding author.
E-mail address: ian.maskery@nottingham.ac.uk (I. Maskery).

https://doi.org/10.1016/j.addlet.2023.100176
Received 29 August 2023; Received in revised form 27 September 2023; Accepted 10 October 2023
Available online 11 October 2023

Renishaw SLM125 PBF-LB system. It was equipped with a 200 W modulated Yb-doped fibre laser ($\lambda \sim 1070$ nm) with a spot diameter at the powder bed of 40 μm. The feedstock was gas-atomised 316L powder with particle size of 15–45 μm, with composition as given in Table 1.

Cubes (10×10×10 mm), standard tensile specimens (4 mm diameter and 20.4 mm gauge length) and tapered tensile specimens (from 4 mm to 5 mm diameter and 20.9 mm gauge length) were fabricated. An optimised PBF-LB process parameter set was employed, as given in Table 2. The effective laser scan speed is given by $v = d/(t_e + t_d)$, where d is the point distance, and t_e and t_d are the exposure time and delay time, respectively. The scan speed was therefore ~ 0.72 m/s.

For the tapered tensile specimen, the geometry was designed to provide a reduction in load-bearing area across the gauge section of 36 % [15]. The resulting local stresses and strains under tensile loading were calculated from finite element analysis (FEA), with the 316L material model based on the stress-strain curve collected from the standard specimen, including post-yield behaviour. FEA was performed using Abaqus/Standard 2021 from Dassault Sistèmes with quadratic tetrahedral elements (C3D10).

The standard and tapered tensile specimens were tested to failure using an Instron 5969 universal testing machine with a 50 kN load cell. The tests were performed at room temperature with a strain rate of 10^{-3} s^{-1}. In both cases, the direction of the tensile load was aligned with the PBF-LB build direction. All samples, standard and tapered, were tested with their surfaces in their as-printed condition. Following fracture, the tapered specimen was cut longitudinally, ground and polished according to standard practice, with a final polish of colloidal silica, to expose the interior for metallurgical analysis.

Vickers hardness tests with a load of 5 kg were carried out using a Buehler Wilson VH3100 automatic hardness tester. The microstructure was characterised with scanning electron microscopy and electron backscatter diffraction (EBSD) using a ZEISS Crossbeam 550 FIB-SEM. EBSD data were collected with a step size of 0.25 μm. The PBF-LB build direction was parallel to the EBSD Z direction. EBSD data were post-processed with the MTEX toolbox in Matlab to evaluate crystallographic phases and texture [16]. Grain boundaries were defined using a threshold of 5°. Twin boundaries (TBs) were defined as Σ3 coincidence site lattice boundaries with a misorientation angle of 60° and rotational axis of ⟨111⟩. A slight angular deviation from the nominal misorientation ($15^\circ/\sqrt{3} = 8.66^\circ$) was accounted for using Brandon's criterion [17]. Twin concentration was determined by the areal fraction of twins observed in the micrographs. Kernel average misorientation (KAM) and Schmid factor maps were used to identify the presence of defects in the material in the plastic regime. KAM maps were used to specify the average misorientation between each measurement point and the nearest neighbours, meaning that the presence of defects in the structure is displayed. As reported in previous work by Gussev et al. [18], KAM maps are used to provide a representation of the distribution of geometrically necessary dislocations in the structure at various strain values. Misorientations exceeding a critical value of 5° were excluded in the calculation.

Lastly, X-ray diffraction (XRD) analysis was performed with a Bruker D8 Advance Da Vinci with a Lynxeye 1D detector. Data was acquired with a step size of 0.02° and a step time of 0.2 s in the range $2\theta = 20^\circ -$ 100 Diffraction peaks were identified using Bruker software Diffrac. EVA.

Results and discussion

A cube of PBF-LB 316L stainless steel was sectioned in the build plane, ground and polished. XRD determined the face-centred cubic crystal structure, while EBSD revealed distinct columnar grains (Fig. 1 (a)), which are a consequence of laser processing, as described by Ma et al. [19]. The grains have a minor preferential orientation of [001] parallel to the BD. A general lack of defects was revealed, with porosity below 0.1 %. Fig. 1(b) illustrates the crystal texture of PBF-LB 316L. The image in the centre shows a preferential {101} fibre texture perpendicular to the BD, while the other two show weak {001} and {111} cubic texture. Etching and microscopy revealed a random orientation of the solidification dendrites, the ones aligned along the BD having a width of 0.57 ± 0.07 μm. A similar value (0.6 ± 0.16 μm) was previously reported for this material by Dépinoy [20]. Fig. 1(c) provides a stress-strain curve obtained from the standard tensile specimen, with the load applied along the BD. The resulting mechanical properties are given in Table 3. The yield strength and ductility are in decent agreement with previous investigations [21]. The strain hardening rate (SHR) curve for the tested standard specimen is shown in Fig. 1(d). This SHR is consistent with previous studies that show presence of twinning, as obtained by Karthik et al. [22].

Fig. 1(e) illustrates the tapered tensile specimen geometry, which was manufactured in PBF-LB 316L and tested to failure, and simulated using FEA to estimate the distribution of local strain. To clarify the role of plastic strain on the microstructure evolution, the tapered specimen was sectioned longitudinally and five regions of interest were chosen along the long axis that showed increasing local plastic strain.

Back-scattered electron imaging was used to examine the selected areas, with the results shown in Fig. 2(a)–(e). Fig. 2(a) shows well defined columnar grains, interrupted only in sporadic areas by twins represented with brighter contrast. In Fig. 2(b) and (c) the density of twins increases, with an evident orientation with respect to the build direction. In Fig. 2(d), the columnar grains are poorly defined, while in Fig. 2(e) the microstructure has been deformed to such an extent that it is not possible to recognise the grains from the starting condition, as in all of them bright twins have emerged. This is in broad agreement with previous studies by Wang et al. and Gao et al. [14,11] which show that plastic strain causes strain-hardening by dislocation slip followed by twin activation.

EBSD in the same regions of the tapered specimen confirmed the presence of deformation twinning. At low strain, twinning is activated only in a subset of grain orientations, in which it is possible to reach the critical shear stress needed to move partial dislocations. For example, it is seen in Fig. 2(f) that grains with the [111] direction parallel to the BD are the first to activate twinning. It is thought that these grains do not reorientate during tensile loading, and therefore the accumulated strain contributes to reaching the critical shear stress necessary for twin activation, as found by Wang et al. [23]. As the strain increases, more grains show twinning activity, as illustrated with arrows in Fig. 2(g). As described by Güden et al. [24] the origin of twins in these grains might be due to a lattice rotation that aligns the [111] crystal orientation to the loading axis, as the tensile load is increased. Below around 15 % strain it is believed that grains with orientations other than [111] mainly experience dislocation slip, as they possess slip systems favourably orientated to the stress state. Finally, as the plastic strain reaches the highest levels, up to ~60 % (Fig. 2(h–j)), the critical shear stress is reached in almost all the grains and peak twin concentration is achieved, as previously identified by Sun et al. [25].

Table 1
Composition of 316L stainless steel powder feedstock, as provided by LPW, ltd.

Element (weight%)											
C	Cr	Ni	Fe	Mo	Mn	Cu	N	O	P	S	Si
0.02	17.8	12.7	Bal.	2.3	0.8	0.02	0.09	0.03	0.008	0.005	0.65

Table 2
PBF-LB process parameters for 316L stainless steel.

Power (W)	Exposure time (μs)	Point distance (μm)	Delay (μs)	Hatch distance (μm)	Layer thickness (μm)	Scanning strategy	Rotation angle (°)
160	50	50	20	50	30	Meander	67

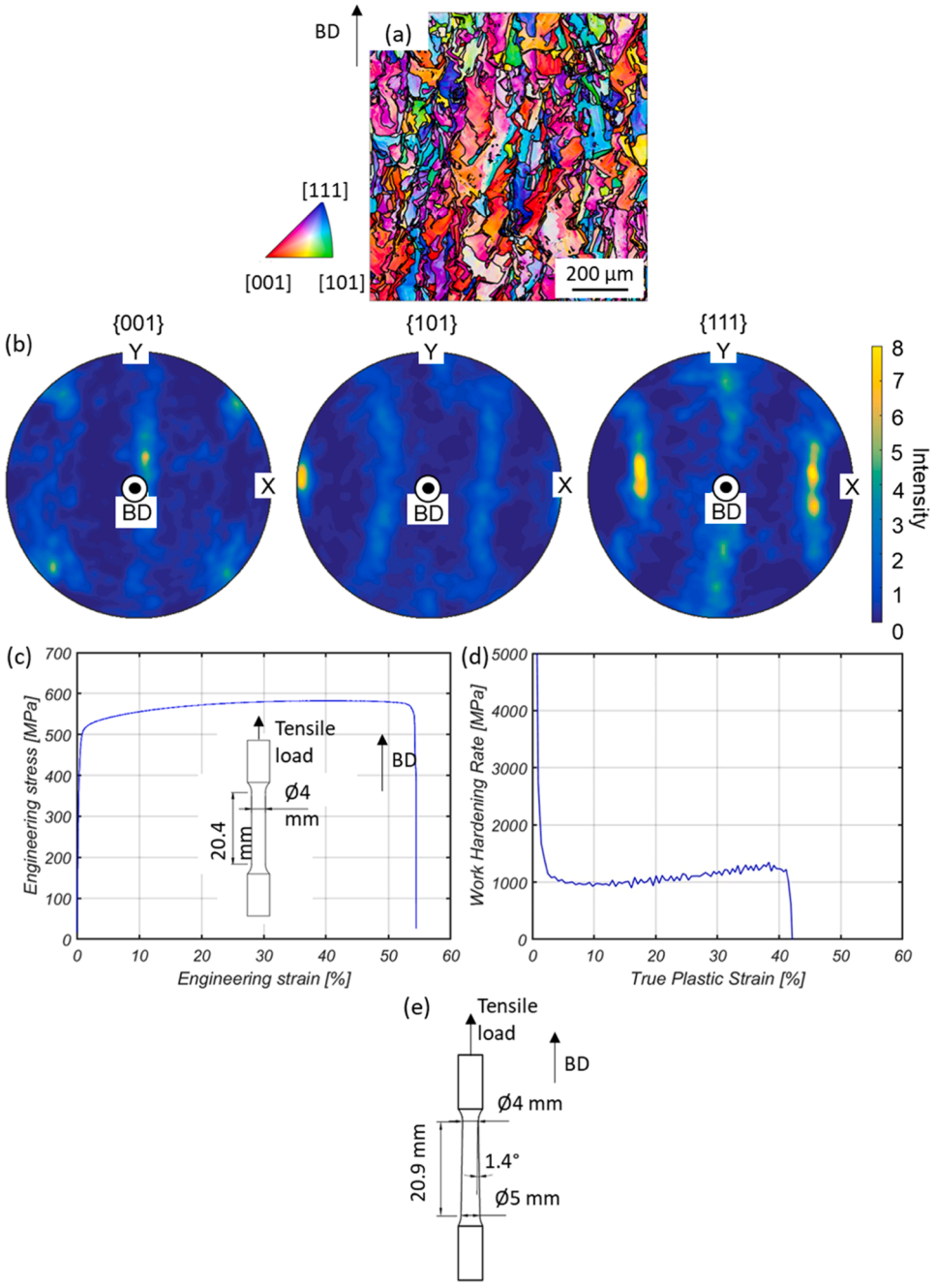

Fig. 1. PBF-LB 316L crystal texture and tensile properties. (a) Z-IPF map; the [100] orientation is aligned with the BD and Z direction. (b) Contour pole figures evaluated along Z//BD. (c) Engineering stress-strain curve from a standard tensile specimen and a drawing of the specimen. (d) strain hardening rate versus true plastic strain plot. (e) Drawing of the tapered specimen.

In Fig. 3(a) the Schmid factor map for the region of the tapered specimen at ≈15 % plastic strain is presented, with the grain orientation defined with the same convention as the EBSD data in Fig. 2. As observed by Bean et al. [26], grains with a low Schmid factor (up to 0.4) present deformation twins. However, this is true only for grains with [111] parallel to the BD. Smaller grains (indicated by red arrows in Fig. 3(a)) and the same low Schmid factor show no noticeable twinning. As described by Barnett [27], the stress at which local yielding occurs increases with decreasing grain size. This means that, in the smallest grains, deformation slip acts instead of twinning. To confirm this experimentally, KAM maps with overlap of the twin boundaries were obtained. The KAM maps are shown in Fig. 3(c) and 3(d) for the 15 %

Table 3
Mechanical properties of 316L stainless steel obtained from standard tensile specimens.

Elastic modulus (GPa)	Yield strength (MPa)	Ultimate tensile strength, UTS (MPa)	Elongation at failure (%)
179 ± 11	485 ± 12	585 ± 5	55 ± 9

plastic strain value. Fig. 3(c) represents a large grain, with [111] orientation, where many twins formed in areas with low KAM values and lower geometrically necessary dislocation distribution. The average KAM in that area is lower than that determined in a smaller grain, with same orientation, displayed in Fig. 3(d). In the smaller grain, deformation slip is the predominant deformation mechanism, as confirmed by only one twin being formed and the presence of many geometrically necessary dislocations within the grain.

The Schmid factor map at ~ 26 % plastic strain, given in Fig. 3(b), shows that the average Schmid factor increased from the ~ 15 % plastic

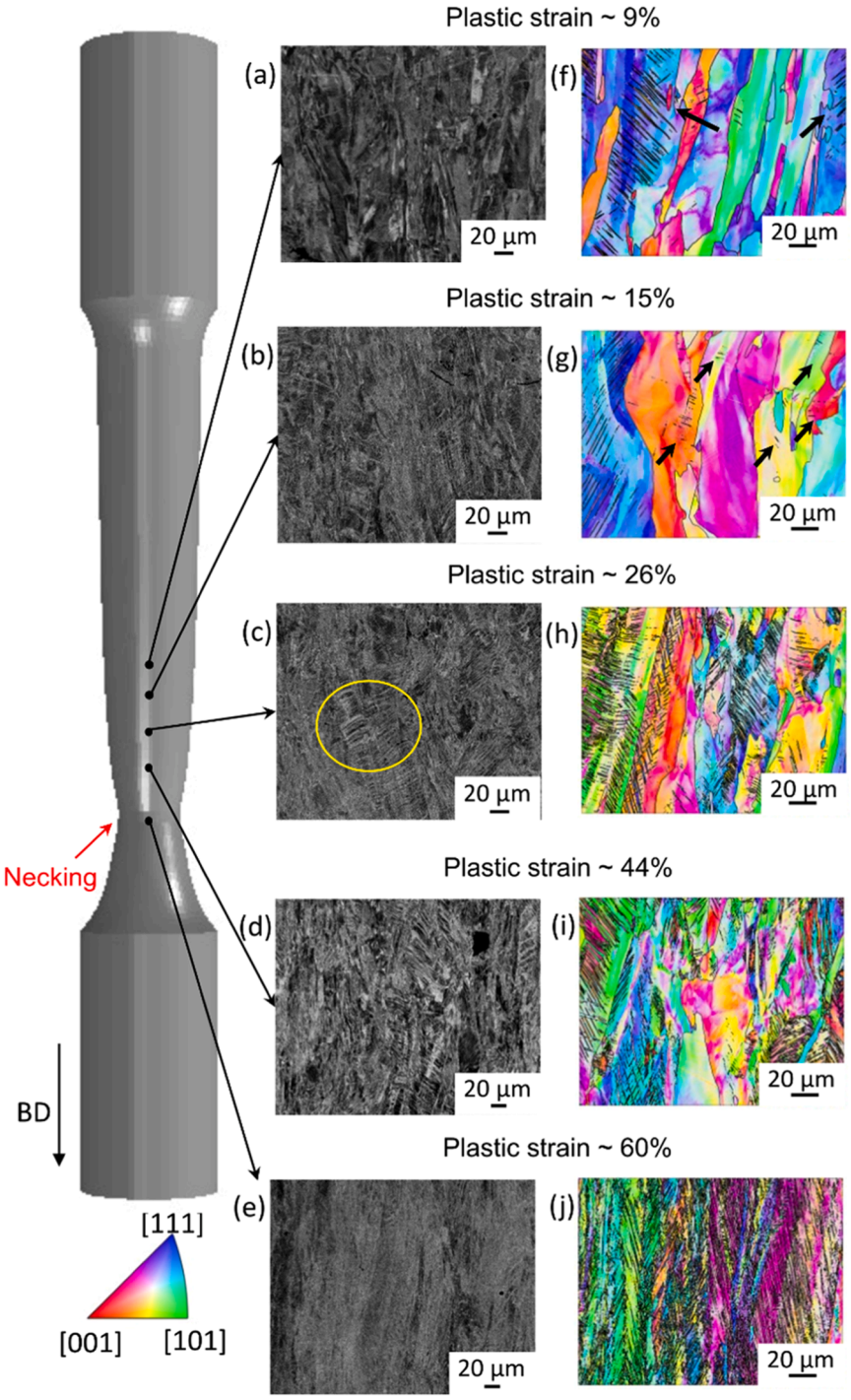

Fig. 2. Microstructural evolution at various strain levels along the axis of the tapered specimen. (a–e) Back-scattered electron images of selected areas of the sectioned tapered specimen covering a range of plastic strain; twins are visible as striations, as circled in (c). (f–j) EBSD maps in the same areas; black arrows indicate grains where twinning is detected.

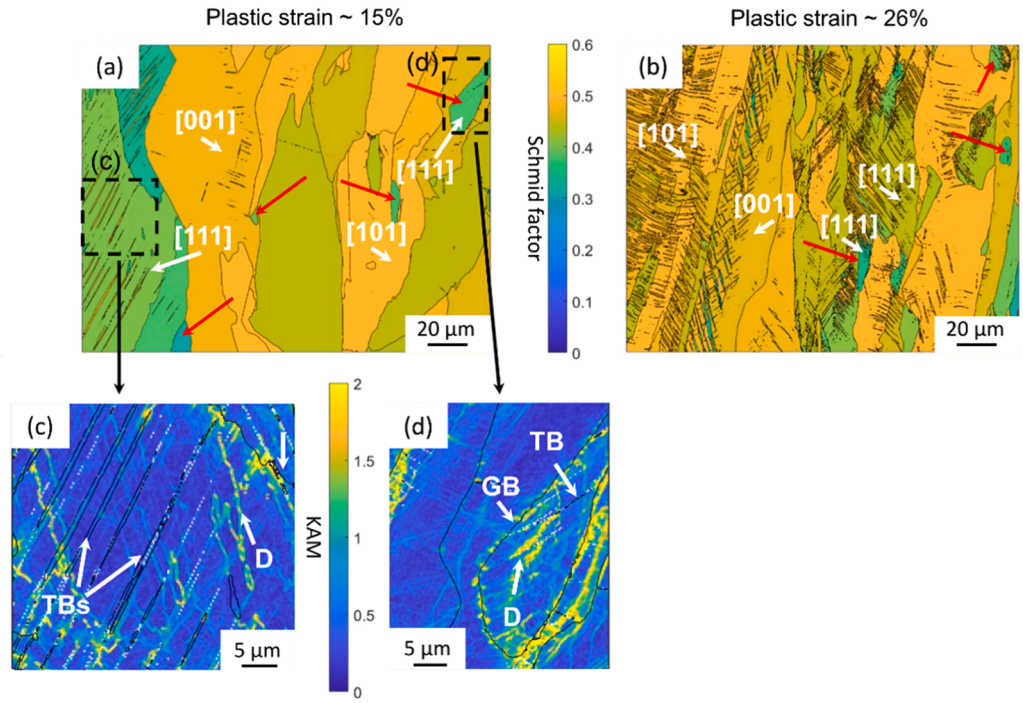

Fig. 3. Schmid factor and KAM maps at increasing plastic strain. (a, b) Schmid factor map for the areas where twinning takes over as predominant deformation mechanism; small grains which do not show twinning are indicated with red arrows. (c, d) KAM maps of two regions highlighted by the dashed boxes in (a), taken from grains with [111] orientation; twin boundaries (TB), dislocations (D) and grain boundaries (GB) are highlighted. (c) is the inset of a large grain, (d) is the inset of a smaller grain.

strain state, and shows a far greater quantity of twins. Fig. 3(b) confirms that, as the strain increased, the next favourable orientations for deformation twinning were [101] followed [001]. This is consistent with the observation from Pham et al. [13] that the [001] grains are the last to form twins because these grains are preferably orientated for dislocation slips. Moreover, as in Fig. 3(a), Fig. 3(b) shows that small grains with [111] orientation do not form twins, thus confirming the importance of grain size in the activation of twinning.

Fig. 4(a) shows the trend of the trues stress versus position along the specimen's axis, zero being the fracture point, while in Fig. 4(b) hardness from the experimental investigation of the tapered sample is given versus position along the specimen's axis. Hardness increased along the axis towards the fracture tip, with the highest value being 380 HV. This demonstrates that significant strain-hardening occurred during deformation. Similarly, the concentration of twins increased along the specimen toward the tip. To provide an overview of the stress trend on the tapered specimen at the point at which the UTS was reached, in Fig. 4(c) is the FEA prediction of the stress. In Fig. 4(d), hardness and twin concentration are expressed in relation to the local strain predicted by FEA. Notably, below 15 % plastic strain the twin concentration is quite stable. In this strain region, twins are believed to occur only within grains where the [111] direction is favourably orientated with the loading direction, meaning the Schmid factor is sufficiently low to produce local twinning [28]. Between 15 % and 26 % strain, a significant increase in twin concentration was observed from around 2 % to 11 % of the examined areas. Then, at 44 % and 60 % strain, the twin concentration rose to 15 % and 28 %, respectively. This behaviour, including an initial low strain phase with low twin concentration followed by a rapid increase of twinning, and finally a twin concentration plateau, was previously observed by Gao et al., who conducted compression tests on additively manufactured 316L [14].

Hardness also increased as a function of strain, with an initial rapid increase in the region up to 15 % strain, from 230 HV to 300 HV. Thereafter, once twinning was activated, a more modest rate of increase was seen, with the peak value reaching 380 ± 10 HV at the fracture tip. As for the localised true stress in the regions between 15 % and 26 % strain, our FEA predicts an increase from 544 MPa to 694 MPa. This is in good agreement with the stress range found by Güden et al. in their examination of 316L also under tensile loading [24]. This means that work hardening occurred after the yield point and slip motion was the responsible mechanism. Twinning therefore became the predominant deformation mechanism only above a threshold strain, which is in keeping with the theoretical concept of twinning activation in strain-hardenable materials put forward by Christian et al. [29].

Conclusions

This report introduces a new methodology to investigate the development of twinning in strain-hardenable 316L stainless steel made by additive manufacturing. A tapered tensile specimen was loaded and brought to failure, providing insights into to the microstructural evolution of the material by inducing a large range of hardness, stress and plastic strain along the loading axis.

The main conclusions of this work are: (1) The tapered specimen allowed the quantification of twin concentration as function of plastic strain in a single sample, at strain levels between 0 % and 60 %. This is particularly important for the design of crashworthy engineering structures, because twins are responsible for extending plastic deformation prior to failure. (2) Below 15 % strain the main deformation mechanism of PBF-LB 316L stainless steel was dislocation movement. Above that threshold, deformation occurred via a combination of dislocations and twinning. Our results show that twinning takes place first in grains with [111] preferentially aligned with the BD, and there is a subsequent progressive activation of twins in otherwise orientated grains; [101] from 26 % strain, followed by [001] at the highest strain. (3) The onset of twinning is regulated not just by grain orientation but also by grain size. It was noticed that amongst grains with the favourable [111] orientation, the largest were the first to develop twins.

The tapered tensile specimen methodology is recommended to examine the evolution of twinning in 316L stainless steel made under

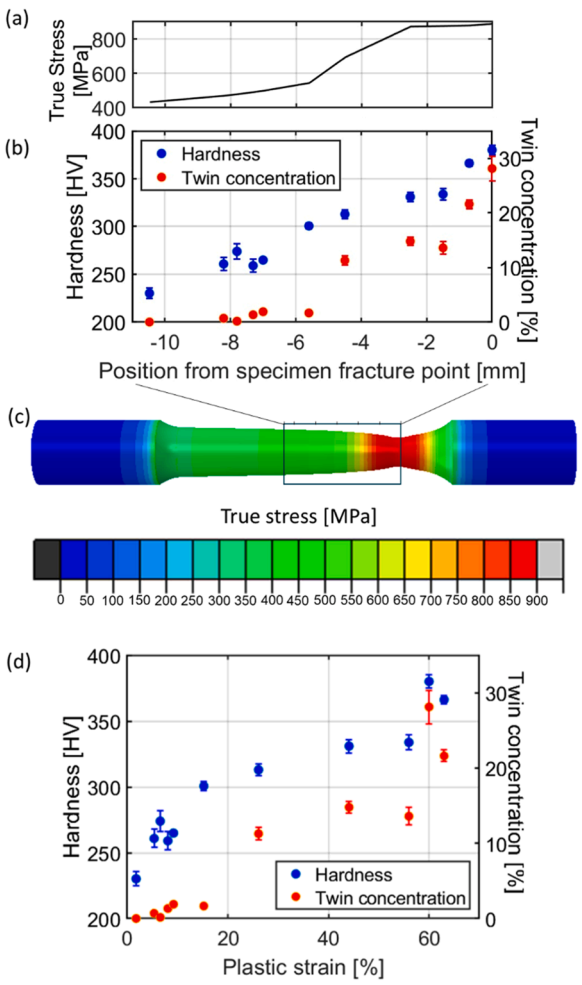

Fig. 4. Stress, hardness and twin concentration in the tapered tensile specimen. (a) FEA true stress line profile data along the tapered specimen from the fracture point for the region highlighted in (c); (b) hardness and twin concentration along the tapered specimen from the fracture point for the region highlighted in (c); (c) Stress distribution in the tapered specimen predicted by FEA at the point of failure; (d) hardness and twin concentration versus plastic strain.

different laser processing conditions; laser scan strategies, power, speed, etc. It may be possible to control the starting grain size distribution and crystal texture, and therefore also the rate at which twinning is activated, through careful selection of processing conditions. Doing so would take engineers one step closer to complete control over 3D form, microstructure and deformation behaviour, and open the additive manufacturing sector to new applications in crash protection.

Data availability statement

The raw/processed data required to reproduce these findings cannot be shared at this time as the data also forms part of an ongoing study.

CRediT authorship contribution statement

D. Della Crociata: Conceptualization, Investigation, Methodology, Writing – original draft. **I. Maskery:** Supervision, Conceptualization, Investigation, Methodology, Writing – review & editing. **R. Hague:** Supervision, Resources, Writing – review & editing. **M. Simonelli:** Supervision, Conceptualization, Investigation, Methodology, Writing – review & editing.

Declaration of Competing Interest

The authors declare that they have no known competing financial interests or personal relationships that could have appeared to influence the work reported in this paper.

Data availability

Data will be made available on request.

Acknowledgments

This work was supported by University of Nottingham (via George Bethell Scholarship). The authors would like to thank the Centre for Additive Manufacturing (CfAM) lab and the Materials lab in Wolfson Building. The authors also thank the Nanoscale and Microscale Research Centre (nmRC) for providing access to instrumentation and Dr Nigel C. Neate for technical assistance; this work was supported by the Engineering and Physical Sciences Research Council (EPSRC) [under grant EP/S0214334/1] and the University of Nottingham.

References

[1] M. Marya, V. Singh, S. Marya, J.Y. Hascoet, Microstructural development and technical challenges in laser additive manufacturing: case study with a 316l industrial part, Metall. Mater. Trans. 46 (2015) 1654–1665, https://doi.org/10.1007/s11663-015-0310-5. B: Process Metallurgy and Materials Processing Science.

[2] D. Hu, R. Kovacevic, Sensing, modeling and control for laser-based additive manufacturing, Int. J. Mach. Tools Manuf. 43 (2003), https://doi.org/10.1016/S0890-6955(02)00163-3.

[3] A.J. Pinkerton, L. Li, Modelling the geometry of a moving laser melt pool and deposition track via energy and mass balances, J. Phys. D Appl. Phys. 37 (2004) 1885–1895, https://doi.org/10.1088/0022-3727/37/14/003.

[4] T. Maconachie, M. Leary, J. Zhang, A. Medvedev, A. Sarker, D. Ruan, G. Lu, O. Faruque, M. Brandt, Effect of build orientation on the quasi-static and dynamic response of SLM AlSi10Mg, Mater. Sci. Eng. A 788 (2020), https://doi.org/10.1016/j.msea.2020.139445.

[5] K. Saeidi, X. Gao, Y. Zhong, Z.J. Shen, Hardened austenite steel with columnar subgrain structure formed by laser melting, Mater. Sci. Eng. A 625 (2015) 221–229, https://doi.org/10.1016/j.msea.2014.12.018.

[6] T. Voisin, J.B. Forien, A. Perron, S. Aubry, N. Bertin, A. Samanta, A. Baker, Y. M. Wang, New insights on cellular structures strengthening mechanisms and thermal stability of an austenitic stainless steel fabricated by laser powder-bed-fusion, Acta Mater. 203 (2021), https://doi.org/10.1016/j.actamat.2020.11.018.

[7] D. Laskowska, T. Szatkiewicz, B. Bałasz, K. Mitura, Mechanical properties and energy absorption abilities of diamond TPMS cylindrical structures fabricated by selective laser melting with 316L stainless steel, Materials 16 (2023), https://doi.org/10.3390/ma16083196 (Basel).

[8] T. Zhong, K. He, H. Li, L. Yang, Mechanical properties of lightweight 316L stainless steel lattice structures fabricated by selective laser melting, Mater. Des. 181 (2019), https://doi.org/10.1016/j.matdes.2019.108076.

[9] Q. Ma, Z. Li, J. Li, Compression behavior of SLM-Prepared 316L Shwartz diamond structures under dynamic loading, Crystals 12 (2022), https://doi.org/10.3390/cryst12040447 (Basel).

[10] M. Ma, Z. Wang, X. Zeng, A comparison on metallurgical behaviors of 316L stainless steel by selective laser melting and laser cladding deposition, Mater Sci Eng. A 685 (2017) 265–273, https://doi.org/10.1016/j.msea.2016.12.112.

[11] Y.M. Wang, T. Voisin, J.T. McKeown, J. Ye, N.P. Calta, Z. Li, Z. Zeng, Y. Zhang, W. Chen, T.T. Roehling, R.T. Ott, M.K. Santala, P.J. Depond, M.J. Matthews, A. V. Hamza, T. Zhu, Additively manufactured hierarchical stainless steels with high strength and ductility, Nat. Mater. 17 (2018) 63–70, https://doi.org/10.1038/NMAT5021.

[12] F. He, C. Wang, B. Han, G. Yeli, X. Lin, Z. Wang, L. Wang, J.J. Kai, Deformation faulting and dislocation-cell refinement in a selective laser melted 316L stainless steel, Int. J. Plast. 156 (2022), https://doi.org/10.1016/j.ijplas.2022.103346.

[13] M.S. Pham, B. Dovgyy, P.A. Hooper, Twinning induced plasticity in austenitic stainless steel 316L made by additive manufacturing, Mater. Sci. Eng. A 704 (2017) 102–111, https://doi.org/10.1016/j.msea.2017.07.082.

[14] S. Gao, Z. Hu, M. Duchamp, P.S.S.R. Krishnan, S. Tekumalla, X. Song, M. Seita, Recrystallization-based grain boundary engineering of 316L stainless steel produced via selective laser melting, Acta Mater. 200 (2020) 366–377, https://doi.org/10.1016/j.actamat.2020.09.015.

[15] H.K.D.H. Bhadeshia, An aspect of the nucleation of burst martensite, J. Mater. Sci. 17 (1982) 383–386, https://doi.org/10.1007/BF00591473.

[16] F. Bachmann, R. Hielscher, H. Schaeben, Grain detection from 2d and 3d EBSD data-Specification of the MTEX algorithm, Ultramicroscopy 111 (2011) 1720–1733, https://doi.org/10.1016/j.ultramic.2011.08.002.

[17] D.G. Brandon, The structure of high-angle grain boundaries, Acta Metall. 14 (11) (1966) 1479–1484, https://doi.org/10.1016/0001-6160(66)90168-4.
[18] M.N. Gussev, K.J. Leonard, *In situ* SEM-EBSD analysis of plastic deformation mechanisms in neutron-irradiated austenitic steel, J Nucl Mater 517 (2019) 45–56, https://doi.org/10.1016/j.jnucmat.2019.01.034.
[19] D. Ma, A.D. Stoica, Z. Wang, A.M. Beese, Crystallographic texture in an additively manufactured nickel-base superalloy, Mater. Sci. Eng. A 684 (2017) 47–53, https://doi.org/10.1016/j.msea.2016.12.028.
[20] S. Dépinoy, Influence of solidification conditions on chemical heterogeneities and dislocations patterning in additively manufactured 316L stainless steel, Materialia 24 (2022), https://doi.org/10.1016/j.mtla.2022.101472 (Oxf).
[21] M. Güden, S. Enser, M. Bayhan, A. Taşdemirci, H. Yavaş, The strain rate sensitive flow stresses and constitutive equations of a selective-laser-melt and an annealed-rolled 316L stainless steel: a comparative study, Mater. Sci. Eng. A 838 (2022), https://doi.org/10.1016/j.msea.2022.142743.
[22] G.M. Karthik, E.S. Kim, P. Sathiyamoorthi, A. Zargaran, S.G. Jeong, R. Xiong, S. H. Kang, J.W. Cho, H.S. Kim, Delayed deformation-induced martensite transformation and enhanced cryogenic tensile properties in laser additive manufactured 316L austenitic stainless steel, Addit. Manuf. 47 (2021), https://doi.org/10.1016/j.addma.2021.102314.
[23] X. Wang, J.A. Muñiz-Lerma, M. Attarian Shandiz, O. Sanchez-Mata, M. Brochu, Crystallographic-orientation-dependent tensile behaviours of stainless steel 316L fabricated by laser powder bed fusion, Mater. Sci. Eng. A 766 (2019), https://doi.org/10.1016/j.msea.2019.138395.
[24] M. Güden, H. Yavaş, A.A. Tanrıkulu, A. Taşdemirci, B. Akın, S. Enser, A. Karakuş, B.A. Hamat, Orientation dependent tensile properties of a selective-laser-melt 316L stainless steel, Mater. Sci. Eng. A 824 (2021), https://doi.org/10.1016/j.msea.2021.141808.
[25] Z. Sun, X. Tan, S.B. Tor, W.Y. Yeong, Selective laser melting of stainless steel 316L with low porosity and high build rates, Mater. Des. 104 (2016) 197–204, https://doi.org/10.1016/j.matdes.2016.05.035.
[26] C. Bean, F. Wang, M.A. Charpagne, P. Villechaise, V. Valle, S.R. Agnew, D. S. Gianola, T.M. Pollock, J.C. Stinville, Heterogeneous slip localization in an additively manufactured 316L stainless steel, Int. J. Plast. 159 (2022), https://doi.org/10.1016/j.ijplas.2022.103436.
[27] M.R. Barnett, A rationale for the strong dependence of mechanical twinning on grain size, Scr. Mater. 59 (2008) 696–698, https://doi.org/10.1016/j.scriptamat.2008.05.027.
[28] D. Zhao, J. Dong, K.Y. Xie, Effect of local twin Schmid factor on the tension twinning activities in a highly textured Mg–3Al–1Zn alloy under different strain paths, MRS Commun. 12 (2022) 217–222, https://doi.org/10.1557/s43579-022-00165-w.
[29] J.W. Christian, S. Mahajant, Deformation twinning, Prog. Mater. Sci. 39 (1995) 1–157, https://doi.org/10.1016/0079-6425(94)00007-7.